



HAL
open science

In situ IR-ATR study of the interaction of nitrogen heteroaromatic compounds with HY zeolites: experimental and theoretical approaches

Ibrahim Khalil, Carlos Celis Cornejo, Karine Thomas, Philippe Bazin, Arnaud Travert, David Pérez-Martínez, Víctor Gabriel Baldovino-Medrano, Jean-François Paul, Françoise Maugé

► To cite this version:

Ibrahim Khalil, Carlos Celis Cornejo, Karine Thomas, Philippe Bazin, Arnaud Travert, et al.. In situ IR-ATR study of the interaction of nitrogen heteroaromatic compounds with HY zeolites: experimental and theoretical approaches. *ChemCatChem*, 2020, 12 (4), pp.1095-1108. 10.1002/cctc.201901560 . hal-02347138

HAL Id: hal-02347138


<https://hal.science/hal-02347138>

Submitted on 26 Nov 2020

HAL is a multi-disciplinary open access archive for the deposit and dissemination of scientific research documents, whether they are published or not. The documents may come from teaching and research institutions in France or abroad, or from public or private research centers.

L'archive ouverte pluridisciplinaire **HAL**, est destinée au dépôt et à la diffusion de documents scientifiques de niveau recherche, publiés ou non, émanant des établissements d'enseignement et de recherche français ou étrangers, des laboratoires publics ou privés.

In situ IR-ATR study of the interaction of nitrogen heteroaromatic compounds with HY zeolites: experimental and theoretical approaches

Ibrahim Khalil^{1*}, Carlos M. Celis-Cornejo², Karine Thomas¹, Philippe Bazin¹, Arnaud Travert¹, David J. Pérez-Martínez³, Víctor G. Baldovino-Medrano^{2,4} , Jean François Paul⁵, Françoise Maugé¹.

¹Univ. Normandie, UNICAEN, CNRS, Laboratoire Catalyse et Spectrochimie (LCS), F-14050 Caen, France.

²Centro de Investigaciones en Catálisis (@CICATUIS), ⁴Laboratorio de Ciencia de Superficies (@Csss UIS) both at Parque Tecnológico de Guatiguará, Universidad Industrial de Santander, Km 2 vía El Refugio, Piedecuesta, Santander, Colombia, 681011.

³ECOPETROL S.A. – Centro de Innovación y Tecnología ICP, Km 7 vía Piedecuesta, A.A. 4185 Piedecuesta, Colombia

⁵Univ. Lille, CNRS, ENSCL, Centrale Lille, UMR 8181 - UCCS - Unité de Catalyse et Chimie du Solide, F-59000 Lille, France.

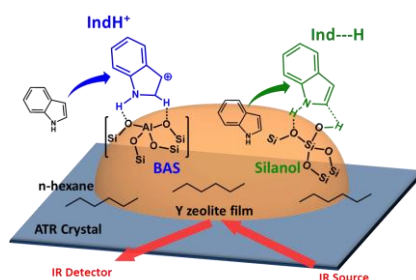
*corresponding author: ibrahim.khalil@ensicaen.fr

Nomenclature

IR-ATR	Infrared Spectroscopy – Attenuated Total Reflectance
DFT	Density Functional Theory
DFT-D3	Zero Damping Density Functional Theory Dispersive Correction
FT-IR	Fourier Transform Infrared Spectroscopy
IRE	Internal Reflection Element
MCT	Mercury Cadmium Telluride detector
PAW	Projector Augmented Wave Method
PBE	Perdew-Burke-Ernzerhof exchange-correlation functional
USY	Ultra-Stable Y Zeolite
VASP	Vienna Ab-initio Simulation Package

1 Table of contents

2



3

4

5 The interaction modes leading to inhibit the hydrocracking catalysts (e.g. zeolites) by the
6 weakly basic nitrogenates, such as indole, were not yet fully understood. The low vapor
7 pressure of these molecules was presenting the inherent difficulty to their study in the gas phase
8 setups. In this work we evidenced, by combining liquid-solid IR-ATR experiments with Density
9 Functional Theory calculations, the vibrational frequencies of the different interaction modes of
10 pyridine and indole with the zeolitic acid sites.

11

1 **ABSTRACT**

2 In the present work, the liquid-solid interaction of liquid N-heteroaromatic compounds,
3 commonly present in the petroleum feedstocks of the refineries, with Y zeolites used in
4 hydrocracking catalysts was followed using IR-ATR spectroscopy. The inhibition of the zeolitic
5 acid sites by strongly basic pyridine as well as by weakly basic indole was highlighted using a
6 continuous flow IR-ATR cell. Results were assessed by Density Functional Theory calculations
7 to compute the vibrational frequencies of pyridine and indole according to the nature of the
8 interaction sites: silanol groups or acidic OH groups. The study points out that IR-ATR
9 spectroscopy opens the way for investigating the interaction modes of low vapor pressure
10 molecules (e.g. indole) that present an inherent difficulty to be operated in the gas phase.
11 Moreover, the IR-ATR makes possible the analysis of the little-explored low wavenumber zone
12 ($< 800 \text{ cm}^{-1}$), that presents informative vibrational modes on the adsorption mode of N-
13 molecules. Hence, this work points out that for pyridine, the bands at 686 and 727 cm^{-1} are
14 characteristic of pyridinium species formed over zeolitic OH groups, meanwhile, the signals at
15 703 and 750 cm^{-1} , are associated to pyridine in interaction with silanol groups. The IR-ATR
16 study reveals that indole, a weakly basic compound, can be protonated on acidic Y zeolites as
17 unambiguously evidenced by the formation of the bands at 1617 , 1608 , 1543 and 705 cm^{-1} .
18 Findings here exposed are crucial for studying inhibitory effects exerted by weak nitrogenated
19 compounds on acidic materials during hydrocracking processes.

20 **KEYWORDS:** IR-ATR *in situ*, organonitrogen compounds, liquid-solid interface, indole,
21 pyridine, zeolite, Brønsted acidity, silanol group, molecular modeling.

22

1. INTRODUCTION

Understanding the adsorption of nitrogen-heteroaromatic compounds over zeolites is a key to improve their design and applications in the chemical industries.^[1] The interaction of nitrogen heteroaromatics with zeolites has been amply studied within the frame of refining processes such as hydroprocessing and hydrocracking.^[2-6] Among these compounds, pyridine and indole-type molecules are commonly present in the petroleum feedstocks of the refineries.^[7] They are recognized to exert inhibitory or poisoning effects over the activity and selectivity of zeolite-based catalysts employed in hydrocracking units.^[8-10] The inhibitory effect induced by strongly basic pyridine type compounds; which possess an electron-pair donor ability, is broadly documented.^[10-12] Nonetheless, the effect of nitrogen heteroaromatics such as indoles (pKa Indole-H⁺/Indole = -3.6), carbazoles, benzocarbazole over hydrocracking catalysts has only been recently put in evidence.^[4,9] Indeed, a previous work confirmed that weakly basic nitrogenates are the most abundant nitrogenates in a hydrotreated vacuum gas oil (ca. 20 ppm of total nitrogen content).^[4] Even at such a low concentration level, these compounds reduced the catalytic activity and influenced the selectivity of the employed catalyst.^[4] However, the interaction mode leading to inhibit the zeolitic acid sites by the weakly basic nitrogenates was not fully understood.

Otherwise, N-heteroaromatic compounds such as indole are also valorized in the synthesis of fine chemical (pharmaceuticals, agrochemicals, and dyes).^[13-20] These reactions are conventionally performed over both liquid phase Brønsted acids and Lewis acids.^[21] However, due to the production of harmful wastes, corrosion issues, and the difficulty of product separation, recent efforts have been made in replacing these substances by zeolites.^[19,20] Indeed, the reaction of indole with zeolitic acid sites was reported for the production of biologically and physiologically active chemicals, by electrophilic or nucleophilic substitutions reactions.^[22] Gopal *et al.* studied the vapor-phase alkylation of indole with methanol to produce 3-methylindole over a series of protonic and rare earth cation exchanged Y zeolites and HZSM-5 zeolites.^[19] The authors reported that the Brønsted and Lewis acid sites of medium strength are

1 key for the performed reaction. Karthik *et al.* investigated the electrophilic substitution over the
2 C3 (carbon 3) atom of indole with aldehydes, using proton exchanged H β , HY, HZSM-5, and
3 Zn ion-exchanged Y zeolites, for producing bis(indolyl)methanes; that are active substances for
4 the promotion of beneficial estrogen metabolism in the human body.^[20] The authors claimed a
5 correlation between the increases of the reaction yield and the amount of Lewis acid sites,
6 assessed by DRIFT measurements of adsorbed pyridine. However, the interaction mode of
7 indole molecules with the active sites in the zeolites was not investigated.

8 In this sense, IR spectroscopy can be used to discriminate the different interaction modes of the
9 molecules with the acid sites of the catalysts.^[23] Most of the work, in which IR spectroscopy
10 characterizations are included, make use of the transmission-adsorption and diffusive
11 reflectance mode of analysis.^[24] Thus, IR cells for *in situ and operando* studies working on
12 transmission mode have been developed for characterizing the different interaction modes of the
13 molecules with the acid sites after specific activation conditions and/or during the reaction.^[23]
14 The feasibility of an IR gas phase study is limited by the vapor pressure of the studied probe
15 molecules. For pyridine, the saturation of solid materials under low pressure conditions is
16 relatively easy to perform since the vapor pressure of the molecule is about 2733 Pa at 298K.^[25]
17 However, when the molecules exhibit low vapor pressures, such as indole and indole-
18 derivatives ($P^{\text{sat}}_{\text{indole}} = 1.6 \text{ Pa}$ at 298K), their handling in the IR *in situ* cell becomes either
19 problematic or unfeasible. In such cases, the characterization with IR-ATR spectroscopy opened
20 a wide range of possibilities for *in situ* studies of liquid-solid adsorption.^[26] Experimental setups
21 concerning IR-ATR continuous flow,^[27–29] batch cells,^[30] and others have been adapted for
22 studying the adsorption of probe molecules in the liquid phase,^[26] as well as for homogeneous
23 and heterogeneous catalytic processes and electrochemical studies.^[31–38] In particular, Rivera *et al.*
24 performed pyridine adsorption in liquid phase over sol-gel films deposited over the ATR
25 crystal solubilized in n-heptane and methanol.^[27] Panella *et al.* used a liquid-solid IR-ATR batch
26 cell to study the reactivity of amino-functionalized silica-coated magnetic nanoparticles of
27 SiO₂/Fe₃O₄.^[30]

1 As a complement to IR spectroscopy experiments, first-principle calculations for the adsorption
2 of probe molecules can provide deeper insights into the mechanisms of adsorption. Figure SI-1
3 depicts the formation of the ion-pair complex for pyridine adsorbed on a model Brønsted site.^{[39–}
4 ^{41]} In this sense, Castellà-Ventura *et al.* described the vibrational modes of pyridine adsorbed on
5 a twelve tetrahedra (12T) cyclic cluster, for modeling the zeolite acid site.^[42] The authors drew
6 attention to the importance of including dispersive interactions in the quantum mechanical
7 model for future studies. Their results were in line with the formation of an ion-pair complex of
8 pyridine H-bonded to the acid site, concluding that the mentioned adsorption mode is
9 energetically more stable than the non-protonated hydrogen-bonded pyridine molecule. Thus,
10 the interest of the theoretical assessment for predicting the characteristic bands in the IR
11 spectrum for a specific interaction of probe molecules was clearly shown. We should mention
12 here that the literature does not report any study of the adsorption of indole molecules on acidic
13 solids.

14 Given the foregoing, in this work, an assessment of the adsorption of pyridine and indole on
15 zeolites via an *in situ* liquid-solid IR-ATR methodology is presented. Two zeolites presenting
16 different Si/Al ratios were studied: namely, HY and USY. Besides, siliceous MCM-41 was also
17 used as a material free of aluminum and with very limited acidic properties. Experiments were
18 complemented by DFT calculations to help in the interpretation of the results.

19 In the first part of the study, the validation of the IR-ATR liquid system was successfully
20 performed by comparing pyridine adsorption in the gas and liquid phases over different solids.
21 The bands relative to the different adsorption modes of pyridine, e.g. over Brønsted acid sites,
22 silanol groups, and Lewis acid sites were distinguished from the characteristic bands belonging
23 to pyridine in the liquid phase. In the second part, the adsorption and protonation of liquid
24 indole, an unfeasible experiment in the IR gas setups, was successfully carried out in the IR-
25 ATR liquid-solid setup. IR-ATR allows also exploring the low wavenumber zone ($<800\text{ cm}^{-1}$)
26 which is generally opaque in classical IR gas analyses, mainly due to the presence of structural
27 vibrations of the studied materials. Combining experiments and DFT calculations provided

1 evidence for the protonation of indole. Thus, the obtained results confirm that the weakly basic
2 nitrogenates such as indole may strongly interact with zeolitic Brønsted acid sites, which
3 explains the inhibitory effect on acid-type reactions reported on zeolite catalysts.^[4,9]

4 **2. EXPERIMENTAL SECTION**

5 **2.1 Studied Materials**

6 Three solids were studied: namely, proton exchanged HY zeolite, Si/Al = 2.5, ultra-stable Y
7 (USY) zeolite, Si/Al = 33, and a siliceous MCM-41. HY zeolite and H-USY were supplied by
8 Union Carbide and Zeolyst International, respectively. Both zeolites were used as provided by
9 the suppliers. MCM-41 was prepared using the procedure of Grün *et al.*, as described in
10 Supporting Information (SI).^[43]

11 **2.2 Assessment of Physicochemical Properties**

12 **Chemical composition.** The silicon and aluminum contents of the zeolites were measured by
13 inductively coupled plasma (ICP) coupled with optical emission spectroscopy using a Varian
14 ICP-OES 720-ES. ca. 50 mg of the solid to analyze was first dissolved in 1 ml of aqua regia
15 ($\text{HNO}_3 / \text{HCl} = 1/3$ v/v) and 3 ml of hydrofluoric acid (Merck, $\geq 48\%$ in water). After 1 h of
16 stirring at 383K, 20 ml of ultra-pure water (VWR, $> 99.99\%$) and 3.6 g of boric acid (Merck,
17 $\geq 99.5\%$) were added. Finally, the solution was diluted until reaching a total volume of 100 ml.
18 The concentrations of Si and Al obtained from ICP-OES are shown in Table 1.

19 **Porosity and surface area.** The porosity and surface area of the solids were estimated from
20 nitrogen adsorption-desorption isotherms measured at 77K using an ASAP 2020 (Micrometrics)
21 gas adsorption system within a relative pressure (P/P_0) range between 0.05 and 1.00. Before the
22 adsorption of nitrogen, samples of ca. 100 g were outgassed at 623K under vacuum for 4 h. The
23 total and external surface areas were determined based on the BET theory for the zeolite
24 samples and on the α -plot method for the mesoporous silica solids,^[44,45] using non-porous silica

1 LiChrospher Si-1000 (surface area = 26.2 m².g⁻¹) as a reference. The corresponding isotherms
2 are shown in supporting information (Figure SI-2).

3 **IR study of the gas probes over the solids.** The evaluation of the acidity of the solids was
4 performed by gas-phase pyridine adsorption followed by Fourier Transform Infrared (FT-IR)
5 spectroscopy. Samples were pressed into self-supported wafer (10 - 15 mg, precisely weighted)
6 with a surface of 2.0 cm² under a pressure of ~10⁷ Pa using a Specac press. These wafers were
7 *in situ* activated under secondary vacuum from 298K to 623K (1 K.min⁻¹) and kept under the
8 latter temperature for 4 h under 10⁻⁴ Pa. FT-IR spectra were recorded after submitting wafers to
9 the latter treatment. The vapor of pyridine was introduced into the cell at 298K and dosed from
10 0.09 to 0.90 μmol. A final equilibrium pressure of 266 Pa was established in the IR cell.
11 Desorption was carried under secondary vacuum (10⁻⁴ Pa) at different steps of temperature until
12 423K for 20 min in each step. FT-IR spectra were recorded with a Thermo Fischer 6700
13 instrument equipped with an MCT detector. 64 scans were accumulated for each measurement
14 with a resolution of 4 cm⁻¹. Spectra were analyzed by subtracting spectra collected after
15 adsorption (or desorption) from the spectra corresponding to the activated samples. All spectra
16 were normalized to a disc constant mass of 5.0 mg.cm⁻² of the dried solids. The amount of acid
17 sites was calculated by integrating the bands related to the residual pyridinium ions (Brønsted
18 sites) and coordinated pyridine species (Lewis sites) after desorption and considering their
19 molar absorption coefficients.^[46]

20 **2.3 IR-ATR Study of the Liquid Probes over the different Materials**

21 The adsorption of solutions of n-hexane with pyridine (1 wt.%) or indole (0.5 wt.%) over the
22 different zeolites and MCM-41 films was studied by *in situ* IR-ATR measurements.

23 The schematics of the home-built continuous flow IR-ATR setup are shown in Figure 1. The
24 cell consists of a dome-like device mounted on the IR-ATR crystal that allows the flow of
25 either gases or liquids streams by a 3-ways valve. The Internal Reflection Element (IRE) was
26 provided with a Specac Golden Gate ATR device along with a diamond crystal and one
27 reflection beam. The IRE was placed in a Nicolet iS50 FTIR spectrometer equipped with

1 nitrogen cooled MCT detector and purged under a flow of dry air without CO₂. Two recipients,
2 one containing the solution with pyridine or indole and another containing the pure solvent were
3 connected simultaneously to a multi-channel peristaltic pump (Ismatec). An additional 3-ways
4 valve was employed for switching from the flow of the solution to the solvent. The solvent
5 employed was n-hexane (99%, Sigma-Aldrich), and the test solutions contained 1 wt.% of
6 pyridine (99.9%, Merck) or 0.5 wt.% of indole (>99%, Sigma-Aldrich). The indole solution was
7 less concentrated due to the low solubility of this compound in non-polar solvents. Finally, a
8 recipient was employed for storing the liquid effluents at the outlet of the IR-ATR cell.

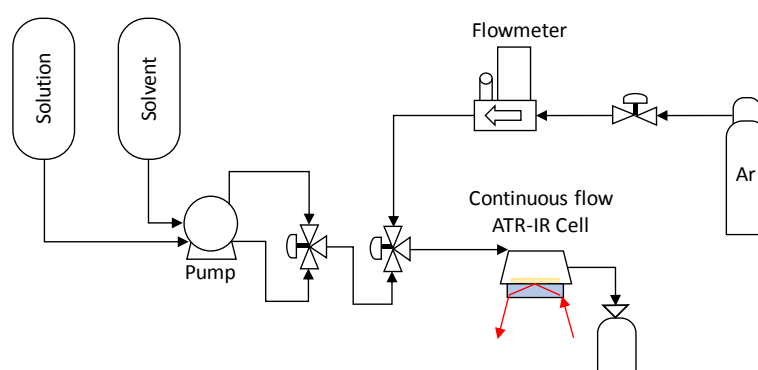


Figure 1. Flowsheet type scheme of the continuous flow IR-ATR cell setup. The solution recipient contains the diluted N-molecule into n-hexane; the solvent recipient contains pure n-hexane.

9 Prior to adsorption tests, a background was always recorded with the empty cell under an Argon
10 flow of 50 ml.min⁻¹. Each spectrum corresponds to the average of 32 scans collected with a
11 resolution of 4 cm⁻¹ (time resolution ~20 seconds). Spectra from the liquid solution and the
12 solvent were recorded. The samples of the zeolites were pretreated *ex situ* at 623K for 4 h under
13 secondary vacuum (10⁻⁴ Pa). The method proposed by Davantès *et al.* was adapted to deposit
14 the solid film of the sample onto the ATR crystal.^[28] Accordingly, a droplet of the concentrated
15 suspension of the pretreated solid, with a granulometry less than 20 μm, was put on top of the
16 IR-ATR crystal and left to dry. Thereafter, the deposited zeolites were dehydrated *in situ* under
17 an argon flow of 30 ml.min⁻¹ at 473K for 4 h. The MCM-41 film was studied without *in situ*
18 activation because of its instability during the treatment. After activation, the system was cooled
19 down to RT, and an n-hexane flow was put in contact with the solid sample, we should mention
20 that, in this step, all the solid films fairly resisted the sheer tension of the liquid flow. From this

1 point onwards, a loop for the acquisition of IR-ATR spectra every 20 s was used to follow the
2 accumulation of n-hexane. The spectrum corresponding to saturation of the solid film by n-
3 hexane was taken as a reference to perform further difference with the spectra corresponding to
4 adsorption of the nitrogen aromatic compounds in solution with n-hexane on the solid film.
5 Afterward, keeping the same flow rate, the flow was switched to the solution containing
6 pyridine or indole until reaching saturation. Finally, the desorption of the weakly or non-
7 adsorbed probe molecules was achieved by switching back the liquid flow to n-hexane for
8 several minutes.

9 **2.4 DFT Calculation of the Frequencies of Organonitrogen Compounds on** 10 **Protonic sites**

11 The molecular level adsorption of the nitrogen heterocycles was assessed by theoretical DFT
12 calculations performed on a Brønsted acid site located at the pore mouth of a model
13 mordenite.^[47] Mordenite was chosen instead of faujasite to save computational resources,
14 because of the considerably reduced number of atoms in the conventional unit cell of the latter;
15 144 atoms for mordenite in comparison to 576 atoms for faujasite, if we compare the pure
16 siliceous structures. In addition, the modeling was a constraint to the adsorption of the
17 organonitrogen compounds on the pore mouth of mordenite. In this regard, the choice of
18 mordenite, which has a 12T main cavity as in the supercage of faujasite, should not significantly
19 affect the calculated vibrational frequencies. Such an assumption is based on a theoretical
20 finding that evidenced that the stretching mode of the O-H group of Brønsted acid sites is not
21 significantly affected by the position of the aluminum atom in the different cavities of the
22 framework.^[48] Additionally, the IR spectra of pyridine adsorption on different Y-zeolites and
23 mordenite showed the characteristic bands of pyridine almost at the same frequency values.^[49] It
24 was also shown that the strength in the acidity, which is well described by the adsorption energy
25 of electron donor basic molecules, is more related to the chemical composition of the zeolite
26 than to its morphology.^[50]

1 Calculations were carried out using the Vienna Ab-initio Simulation Package (VASP)
2 considering periodic boundary conditions and pseudo potentials.^[51-53] The Projected Augmented
3 Wave (PAW) method and the Perdew-Burke-Ernzerhof (PBE) exchange-correlation functional
4 were chosen for performing all the calculations.^[54-56] An energy cut-off of 600 eV was set with
5 a Γ -point for sampling the Brillouin-zone. Gaussian smearing with a sigma parameter of 0.05
6 was chosen. Grimme's density functional dispersive correction with zero dampings (DFT-D3)
7 was included to account for dispersive interactions.^[57,58] The external surface of the (001) plane
8 of a mordenite zeolite was modeled following the procedure described in previous work.^[59] The
9 Brønsted acid site at the pore mouth was simulated by replacing one silicon atom for an
10 aluminum one, and subsequently hydrogenating the adjacent oxygen atom for compensating the
11 charge. The T2 position of the Brønsted acid site on the twelve tetrahedra principal cavity was
12 chosen following Demuth *et al.* assumption that this represents the most stable configuration.^[60]
13 Terminal silanol groups were created when completing with hydrogen atoms the dangling
14 oxygen atoms bonds that are generated when the 001 plane is cut. A vacuum of 10 Å in the z-
15 axis is added. The optimized 193-atom structure of the external surface of mordenite is shown
16 in supplementary information (Figure SI-3). The acidic characteristics of the modeled Brønsted
17 site in the pore mouth of the mordenite were validated in previous work,^[59] calculating the
18 vibrational frequency of the O-H group adjacent to the aluminum atom, and the atomic charge
19 of the hydrogen atom. A charge of +0.65 and a frequency of $3604 \pm 5 \text{ cm}^{-1}$ was taken to
20 represent the characteristics of a Brønsted acid site.^[48,61]

21 For studying the adsorption of the probe molecules, pyridine and indole were first optimized in
22 a vacuum cube box with an edge length of 25 Å and a frequency calculation was subsequently
23 performed for obtaining the data of the isolated gas-phase molecules. The predicted vibrational
24 frequencies (not scaled) for pyridine and indole in the gas phase, interacting with the silanol
25 groups or with protonated OH groups of the zeolite were calculated. The interaction of pyridine
26 and indole over a Lewis acid site was not computed in this work. The protonation of indole was
27 performed over the carbon in the position 3 of the molecule (C3 site), known and checked to be

1 the site with the highest proton affinity (PA) from all the 7 sites where the protonation is
2 possible ($PA_{(C3 \text{ protonation})} = 212.4 \text{ kcal/mol}$).^[62]

3 **3. RESULTS AND DISCUSSION**

4 **3.1 Chemical and Textural Properties of the Solids**

5 Table 1 presents the chemical composition and textural properties of the different materials.
6 From ICP results, the Si/Al ratio of the zeolites were calculated. An increase in the Si/Al ratio
7 for the zeolite USY33 containing less aluminum than HY2.5 is observed. The mesoporous
8 volume of the USY zeolite is higher in comparison to the HY2.5 zeolite due to the partial
9 destruction of the structure during the aluminum extraction procedure performed by the
10 supplier. The measured chemical and textural properties of the zeolites are similar to the
11 characterization results obtained for these materials in the literature.^[63–66] The MCM-41 solid
12 did not present any microporosity as shown in Table 1 and Figure SI-2 (nitrogen sorption
13 isotherms), also the obtained surface area, calculated using the α -plot method, was around 1000
14 $\text{m}^2\cdot\text{g}^{-1}$ which is in a good agreement with the results shown by Grün *et al.*^[43]

15 **Table 1. Chemical composition and textural properties of the different materials**

Adsorbents	ICP results ($\text{mg}\cdot\text{g}^{-1}$)		Surface area ^a ($\text{m}^2\cdot\text{g}^{-1}$)	Pore volume ($\text{cm}^3\cdot\text{g}^{-1}$)		
	Si	Al	Total	total	micro	meso
HY 2.5	260.1	102.1	1063	0.39	0.36	0.03
USY 33	412.5	12.5	928	0.47	0.28	0.19
MCM-41	380.1	0.0	984 ^b	0.65	0.00	0.65

16 ^a Nitrogen sorption

17 ^b Determined using α -plot^[45]

18 **3.2 Pyridine Adsorption**

19 **3.2.1 IR Study of the Adsorption of Gas phase Pyridine over the Solids**

20 In a first step, the acid sites were studied by pyridine gas phase adsorption on the solids
21 activated *in situ* at 623K. The IR spectra of the adsorbents before pyridine adsorption are shown
22 in Figure SI-4 and commented in the Supplementary Information. Figure 2 presents the IR

1 spectra of the pyridine species remaining after *in situ* desorption at 423K under secondary
 2 vacuum. The results show the presence of two interaction modes of pyridine with the acid sites.
 3 The band at 1545 cm⁻¹ (ν_{8a} mode) is characteristic for pyridinium ions PyH⁺ formed over
 4 Brønsted acid sites, while the band at 1455 cm⁻¹ (ν_{19b} mode) reveals coordinated pyridine (LPy)
 5 over Lewis acid sites (Figure 2).^[63,67] The observed band at 1490 cm⁻¹ is characteristic of the ν_{19a}
 6 mode over both Brønsted Acid Site (BAS) and Lewis Acid Site (LAS), although its sensitivity
 7 to the concentration of BAS is higher.^[68] The concentration of both BAS and LAS can be
 8 calculated from the integration of ν_{8a} and ν_{8a} bands, respectively, using the following absorption
 9 coefficients: ε_(PyH⁺) = 1.8 cm.μmol⁻¹ and ε_(LPy) = 1.5 cm.μmol⁻¹.^[46]

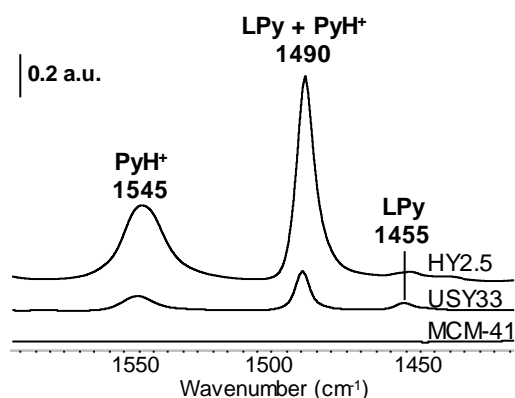


Table 2. Concentration of acidic sites in the different materials

Adsorbents	Acid sites (μmol.g ⁻¹)		
	BAS	LAS	Total
HY2.5	1263	22	1285
USY33	98	61	159
MCM-41	0	0	0

Figure 2. IR spectra of the residual pyridine species over the different solids after desorption at 423K under secondary vacuum.

10
 11 Table 2 shows that the amount of BAS strongly decreases on USY33 as compared to HY2.5,
 12 whereas, the amount of LAS increases due to the formation of extraframework aluminic phase
 13 species during the dealumination treatment.^[69,70] Over MCM-41, which only presents weak-
 14 acidic silanol sites, no acid sites were evidenced after the pyridine desorption at 423K. These
 15 results confirm that the studied solids present various properties in terms of nature and
 16 concentration of acid sites that can serve as references to validate the characterizations
 17 developed herein.

18 3.2.2 IR-ATR Study of Liquid phase Pyridine Adsorption over the Solids

3.2.2.1 IR-ATR study

IR-ATR spectra of the thin films of Y zeolites and MCM-41 after deposition are shown in Figure 3. It must be underlined that for IR analysis in transmission and diffusion modes, of a self-supported silica-based wafer, the structural vibration bands of the solids make the zone below 1200 cm^{-1} almost completely opaque.^[69] By contrast, as shown in Figure 3, these bands present limited intensities in the IR-ATR spectra of thin films, which allows their analysis. For the zeolite samples, the bands in the region at $850\text{--}650\text{ cm}^{-1}$ are characteristic of the mix of the symmetric stretching and bending modes of the T-O-T bridges (ν_2). Also, these bands shift up, the lower is the Al content, as shown for the bands at 789 and 724 cm^{-1} over the HY2.5 zeolite that shift up to 831 and 787 cm^{-1} over the low aluminum loaded USY33 zeolite.^[69] However, it should be noted that probe molecule adsorption can induce distortion at the surface of the solids that can shift the wavenumbers of these structural bands. Thus, positive - negative bands can appear on the difference spectra. Hence, caution must be taken for the interpretation of the bands detected in this low wavenumber zone after the adsorption of pyridine or indole.

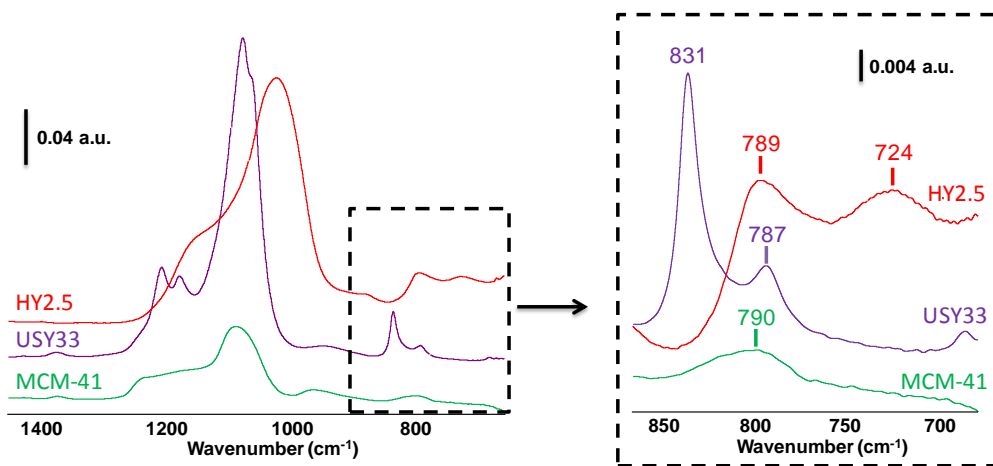


Figure 3. IR-ATR spectra of the thin films of zeolites and MCM-41 as-deposited on the ATR crystal.

15

In general, in IR-ATR mode, all the IR bands as well as those corresponding to the adsorbed species present very low intensities due to the limited thickness of the samples that are analyzed (a few microns). Thus, cautions must be taken in order to avoid any artifacts that can hide the

1 bands coming from adsorption. Among them, one may mention that it is important to watch the
2 stability of the concentration of water present as a contaminant in the purge of the spectrometer
3 during the experiment. Special care must be taken for spectral analysis of the region between
4 1400 and 1600 cm^{-1} where IR bands of water are very intense.

5 **3.2.2.2 IR-ATR study of the liquid phase pyridine - solid interaction**

6 IR-ATR spectra of the liquid pyridine adsorption over the films of HY2.5, USY33, and MCM-
7 41 are presented in Figure 4. The figure compares the spectra of (1) the solution of pyridine in
8 n-hexane (dotted line), (2) the steady-state adsorption of liquid pyridine on the solid film (solid
9 line) and (3) the strongly-adsorbed pyridine species after removing the weakly or non-adsorbed
10 species by flushing the solid film with n-hexane (dashed line). The presented spectra are
11 difference spectra. Spectra (1) are obtained by subtraction the liquid n-hexane spectrum from
12 the spectrum of the solution of pyridine in n-hexane; spectra (2) are obtained by subtraction of
13 the spectra of pure hexane in interaction with the different solid films from the spectra
14 corresponding to the steady-state pyridine adsorption on the different solid films; spectra (3) are
15 obtained by subtraction of the spectra of pure hexane in interaction with the solid films from the
16 spectra recorded after flushing the solid films with n-hexane.

17 Over HY2.5 and USY33 zeolites (Figure 4-A and B), a large increase in the intensities of the
18 pyridine bands after adsorption is observed after comparing with the spectra recorded for the
19 liquid phase pyridine. This indicates an accumulation of pyridine molecules on the solid films
20 and confirms the adsorption phenomenon. Over the MCM-41 film, the adsorption of pyridine is
21 limited as it is indicated by the low intensity of the bands after pyridine adsorption. For the three
22 solids, the spectra show new bands when compared to those of liquid pyridine. The IR-ATR
23 spectra analyses were divided into 2 sections based on the wavenumber zones: high
24 wavenumber zone (1650-1400 cm^{-1}) and low wavenumber zone (800-650 cm^{-1}).

25

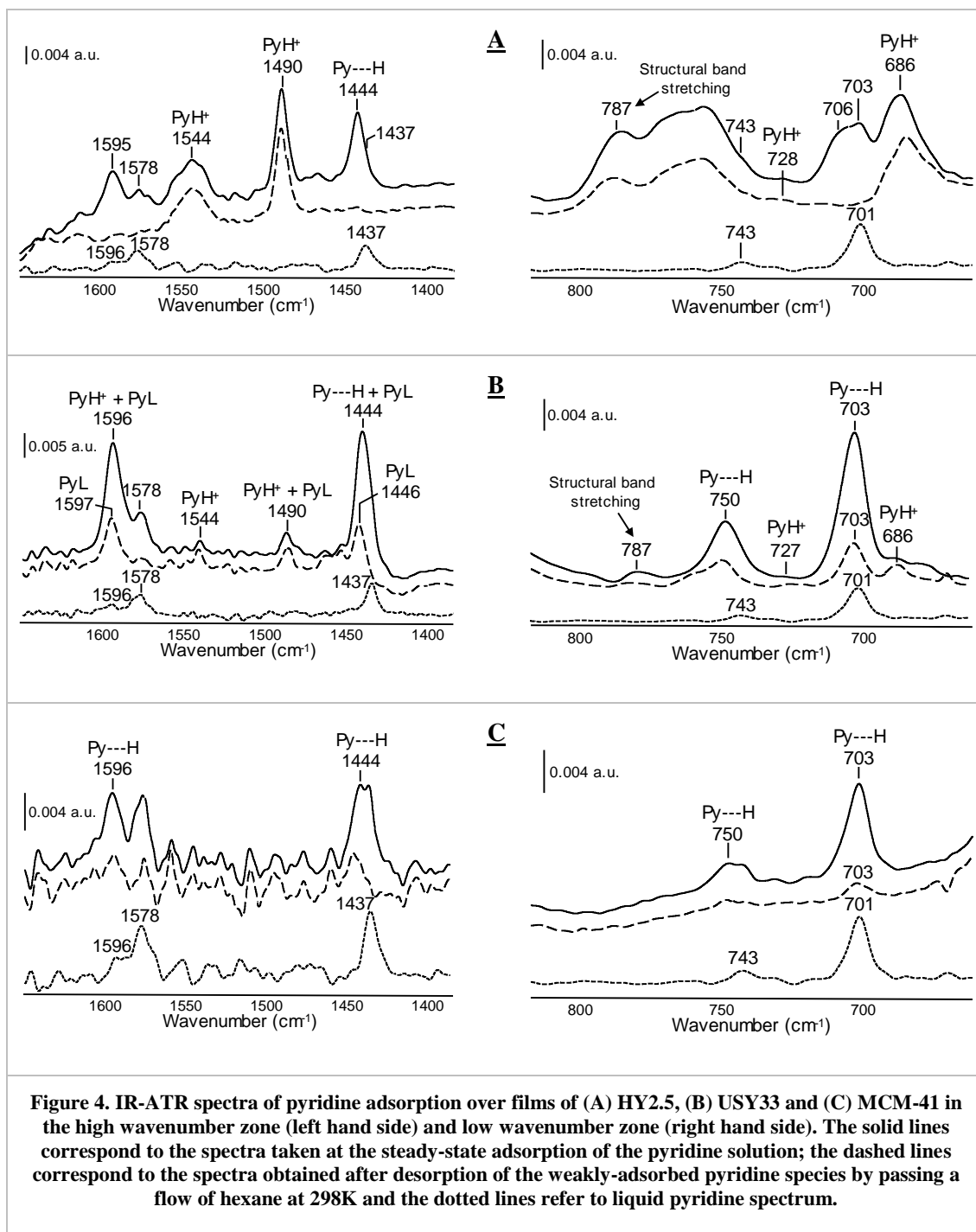


Figure 4. IR-ATR spectra of pyridine adsorption over films of (A) HY2.5, (B) USY33 and (C) MCM-41 in the high wavenumber zone (left hand side) and low wavenumber zone (right hand side). The solid lines correspond to the spectra taken at the steady-state adsorption of the pyridine solution; the dashed lines correspond to the spectra obtained after desorption of the weakly-adsorbed pyridine species by passing a flow of hexane at 298K and the dotted lines refer to liquid pyridine spectrum.

1

2 **High wavenumber zone analysis (1650-1400 cm^{-1})**

3 The spectrum of adsorbed pyridine on the HY2.5 zeolite (Figure 4A - solid line) presents bands
 4 at 1544 and 1490 cm^{-1} , which characterize pyridinium ions formed over BAS. These bands
 5 remain after flushing with the solvent (Figure 4A - dashed line), hence confirming that they
 6 correspond to strongly adsorbed species. The bands at 1595 and 1444 cm^{-1} were attributed to

1 weakly H-bonded pyridine molecules (Py---H) with the solid,^[71,72] this adsorption mode did not
2 resist the desorption under n-hexane flow. The bands for liquid pyridine were also detected
3 during the adsorption (1578 and 1437(shoulder) cm^{-1}), however, they were also eliminated
4 during the desorption.

5 Adsorption results obtained over USY33 are shown in Figure 4B. The bands related to
6 pyridinium ions (Figure 4B - solid line) are present at similar positions than over the HY2.5
7 zeolite (1544 and 1490 cm^{-1}). Note that the intensity of the BAS bands is less than on HY2.5 as
8 expected from the lower Al amount of USY33 (Table 1). The bands at 1597 and 1446 cm^{-1}
9 indicate the presence of LAS on this partially dealuminated zeolite (Table 2).^[63] This
10 assignment is confirmed by the stability of these species under flowing hexane. In addition, the
11 bands of pyridine interacting with silanol groups (1596 and 1444 cm^{-1}) and liquid phase
12 pyridine (1578 and 1437 cm^{-1}) were also detected. However, these bands disappeared by
13 flushing with n-hexane (Figure 4B - dashed line).

14 Over the MCM-41 film, pyridine bands are not intense (Figure 4C - solid line), even being hard
15 to tell them apart from the spectral noise. The spectra mainly exhibit the bands for liquid
16 pyridine. Only two bands at 1596 and 1444 cm^{-1} indicate the formation of weakly-adsorbed H-
17 bonded pyridine species. Rivera *et al.* reported a similar pattern for pyridine adsorption in the
18 liquid phase on silica,^[27] which allowed observing mainly the characteristic bands of liquid
19 pyridine. They reported the appearance of one weak band at 1492 cm^{-1} attributed to pyridinium
20 ions, indicating the presence of strong acid sites. This suggests some Al contamination in the
21 silica. These authors also highlighted the presence of noise in the spectra ascribed to water in
22 the vapor phase that distorts the spectra between 1600 and 1400 cm^{-1} , which makes difficult to
23 distinguish pyridine bands in this region.

24 The acidic site nature of the solids detected by pyridine under liquid phase is in good agreement
25 with that obtained with pyridine under gas phase (section 3.2.1 - Table 2). It is not possible to
26 make a quantitative assessment of the acidic sites by IR-ATR due to the absence of accurate
27 knowledge of the volume of solids probed by the ATR signal. However, a comparison of the

1 ratio between the various pyridine species formed over the tested solids in the gas and liquid
2 phases experiments can be done. The ratios of the areas of the bands located at 1490 cm^{-1} (H-
3 bonded and coordinated pyridine) and 1544 cm^{-1} (protonated pyridine) were compared for
4 pyridine adsorption performed in the gas-solid conditions in the IR transmission set up (areas
5 measured after pyridine evacuation at 423K) (Figure 2) and performed in the liquid-solid with
6 IR-ATR set up (areas measured under hexane flow) (Figure 4). Note that the widespread of the
7 noise across the IR-ATR spectra limits an accurate measurement of the band area. The ratios
8 reach values of 1.3 (gas experiment) and 1.5 (liquid experiment) over USY33. Over HY2.5
9 zeolite, the ratios for gas and liquid experiments were, even more, close with a value of almost
10 1.1 in both experiments. A good agreement between gas and liquid phase adsorption of pyridine
11 is thus shown.

12 ***Low wavenumber zone analysis ($800\text{-}650\text{ cm}^{-1}$)***

13 The study of the zone from 650 to 800 cm^{-1} presents the great advantage to overcome the
14 problem of the spectral noise induced by the water present in the vapor purge. Indeed, water
15 vapor does not present any vibration-rotation bands in this zone and IR-ATR allows the analysis
16 of this spectral zone for thin films of zeolites and oxides. However, as mentioned previously,
17 some solid structural bands are detected in the region of low-frequency ($800 - 650\text{ cm}^{-1}$) (Figure
18 3) and these bands can be shifted by structural distortion due to pyridine adsorption on the solid.
19 This warns that caution should be taken for the interpretation of the bands in this zone. As for
20 the HY2.5 zeolite, an assignment of bands characteristic of weakly adsorbed species or non-
21 adsorbed ones can be proposed by comparing pyridine spectra obtained before and after flowing
22 hexane regarding the spectrum of liquid pyridine (Figure 4A - right). Hence, the band at 706 cm^{-1}
23 can be attributed to H-bonded pyridine, while the bands at 743 and 703 cm^{-1} are related to
24 pyridine in the liquid phase. The strong band at 686 cm^{-1} that resists to hexane flushing likely
25 accounts for pyridinium species. However, due to the presence of strong (str) structural bands
26 between $800\text{-}740\text{ cm}^{-1}$ on HY2.5 (Figure 3), the bands detected at 787 (str), 760 (str), 728 (w-
27 weak) cm^{-1} after pyridine adsorption can arise from a shift of the structural band or pyridine

1 species. Their assignment being shaky with only experimental data, pyridine adsorption
2 frequencies were computed by DFT calculation to validate the proposed assignments (see next
3 section).

4 On USY33 zeolite, the structural bands present limited intensity in the region below 780 cm^{-1}
5 (Figure 3), allowing an easier assignment of the pyridine adsorption bands on this solid. During
6 the adsorption of pyridine, new bands appear at $750(\text{str})$, $727(\text{w})$, $703(\text{str})$, $686(\text{m-medium})\text{ cm}^{-1}$
7 (Figure 4B and its zoom in Figure 5). The intense bands at 750 and 703 cm^{-1} , that are partially
8 eliminated by flushing, can be assigned to pyridine adsorbed over silanol groups. This is in good
9 agreement with the assignment proposed in the previous section. The bands detected at 727 and
10 at 686 cm^{-1} whose stability under flushing is clearly observed in Figure 5, should characterize
11 protonated pyridine as proposed on HY2.5 zeolite. A more robust assignment will be done after
12 comparison with the frequencies calculated by DFT (section 3.2.3).

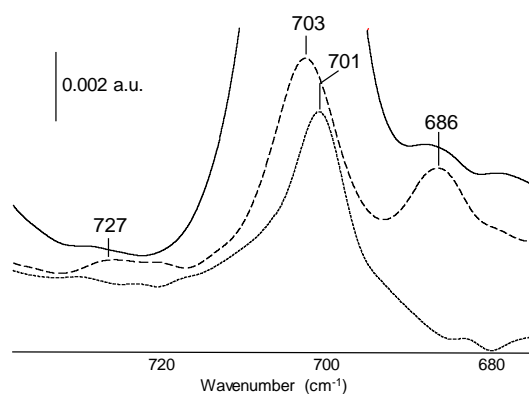


Figure 5. IR-ATR spectra of pyridine adsorbed on USY33 and comparison with pure pyridine (zoom of the Figure 4B right). The solid line corresponds to the steady-state adsorption of the pyridine solution; the dashed line corresponds to the spectrum obtained after desorption of the weakly adsorbed species by passing a flow of hexane at 298K and the dotted line refers to liquid pyridine spectrum.

13 In summary, a good agreement was observed between pyridine adsorption in gas and liquid
14 phases. However, IR-ATR spectra present low intense bands, and the analysis of the region
15 between 1600 and 1400 cm^{-1} was difficult due to the presence of water bands as a contaminant
16 in the spectrometer gas purge.^[27,30] Nevertheless, an advantage of the IR-ATR setup is in giving
17 access to analyze the low wavenumber zone ($800 - 650\text{ cm}^{-1}$), where no water bands appear.
18 Pyridine exhibits some intense bands in this zone that provide interesting information about the

1 adsorption mode of pyridine in the liquid-solid IR-ATR analysis.^[73] To go further, DFT
2 calculations were performed in order to predict expected frequencies according to the
3 interaction mode of pyridine with the surface.

4 3.2.3 Theoretical Assessment of the Adsorption of Pyridine

5 Most of the IR studies using pyridine for probing the acid sites focus on the region between
6 1400 and 1700 cm^{-1} . The corresponding in-plane atomic displacements for the pyridine
7 vibrational modes appearing in this wavenumber zone (ν_{8a} , ν_{8b} , ν_{19a} and ν_{19b}) are shown in
8 Figure 6.^[74] Our work points out the interest of accurately analyzing the vibrational zone
9 between 800 and 600 cm^{-1} for helping in understanding the interaction between liquid pyridine
10 and the solid films. Within the low-frequency zone, ν_{10b} and ν_{11} modes are two characteristic
11 signals of pyridine that correspond to out-of-plane motions (Figure 6).

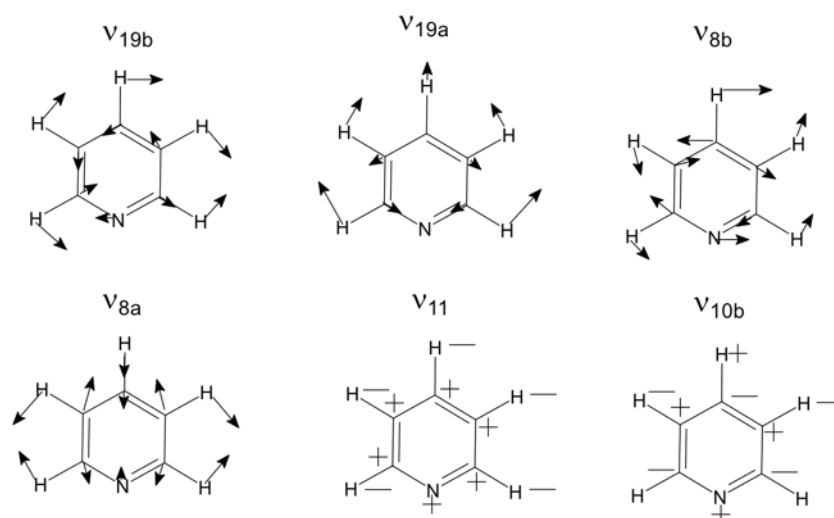


Figure 6. Atomic displacements for the commonly studied vibrational modes of pyridine.

12 Table 3 gathers the frequencies in the high-wavenumber and low-wavenumber zones calculated
13 by DFT for the various vibration modes of gas-phase pyridine, H-bonded, and protonated
14 pyridine. The frequencies of coordinated pyridine molecules over a Lewis acid site were not
15 computed in this work. Table 3 also compares the theoretical and experimental frequencies
16 obtained in this work to theoretical frequencies found in the literature.^[42] In general, a good
17 agreement appears between the frequencies calculated for pyridine in the gas phase and those

1 for pyridine adsorbed over the various sites. The calculations show that H-bonding leads to
 2 limited changes in wavenumbers compared to pure pyridine. This agrees with the fact that the
 3 interaction of pyridine with a silanol can be described as physical adsorption.

4 In the high-wavenumber zone, the vibrational frequencies predicted for pyridine on silanol
 5 groups are in good agreement with the values obtained experimentally (Table 3). For this kind
 6 of interaction, the characteristic vibrations of the pyridine molecules are very similar to those
 7 observed for pyridine in the gas phase. Only when the interaction is strong enough, a
 8 chemisorbed complex of pyridine on a Brønsted site, some changes are observed in the motions
 9 of the pyridine molecules.^[42,75] These changes could explain the registered shifts which are
 10 characteristic of the ion-pair H-bonded complexes described in the literature.^[42,76]

11 For the interaction of pyridine with the Brønsted acid sites, the predicted shifts of the vibrational
 12 modes ν_{8a} and ν_{19a} were similar to what was previously reported in the literature.^[42] However,
 13 for the ν_{8b} and ν_{19b} , vibration modes, the previously calculated values were slightly higher as
 14 compared to the experimental data.^[42] The computed values obtained herein are more realistic
 15 (Table 3). Previous calculations considered a 12T_{OH} size cluster,^[42] while in the present work
 16 the adsorption occurs on a Brønsted acid site located in the pore mouth of a 193-atom
 17 mordenite.

18 **Table 3. Comparison between the predicted vibrational frequencies and the experimental values obtained in**
 19 **IR-ATR for pyridine adsorption over silanol groups and Brønsted acid sites.**

Vibrational mode*	Pyridine frequencies (cm ⁻¹)							
	Gas phase		Silanol group			Brønsted site		
	Other [†] (Calc.) ^[42]	This work (Calc.)	Other [†] (Calc.) ^[42]	This work (Calc.)	This work (IR-ATR)	Other [†] (Calc.) ^[42]	This work (Calc.)	This work (IR-ATR)
<i>8a</i>	1595	1587	1612	1595	1597	1634	1634	-
<i>8b</i>	1591	1574	1591	1573	1578	1669	1621	-
<i>19b</i>	1445	1432	1464	1437	1444	1563	1547	1544
<i>19a</i>	1486	1472	1487	1475	1485	1486	1485	1490
<i>11</i>	-	742	-	745	750	-	721	728
<i>10b</i>	-	699	-	706	703	-	686	686

1 *Wilson's numbers for the vibrational modes of the benzene ring. † Theoretical data from other work,
2 calculated for the pyridine interaction on a Brønsted acid site in a 12T_{OH} zeolite cluster using the
3 *B3LYP/6-31G(d,p)*, as reported in reference.^[42]

4 This work presents, as far as we know, the first calculation of the vibrational frequencies of
5 pyridine in the region of low-frequency (800 – 650 cm⁻¹). Two intense bands were observed:
6 ν_{10b} and ν_{11} , which correspond to out-of-plane vibrations (Figure 6). For the ν_{10b} and ν_{11} modes
7 over a silanol, a small shift was found with bands predicted at 745 and 706 cm⁻¹. This agrees
8 with the observation done for liquid pyridine adsorption over the MCM-41 film (H-bonded
9 bands at 750 and 703 cm⁻¹). Meanwhile, for the interactions with a Brønsted site, characteristic
10 bands at 728 and 680 cm⁻¹ of pyridinium species are predicted.^[73] Hence, based on the
11 calculated frequencies of pyridine chemisorbed on Brønsted sites, the bands observed at 727
12 and 686 cm⁻¹ during the IR-ATR analysis of liquid pyridine – zeolite interaction (Figure 4) can
13 be assigned to pyridinium species.

14 In summary, a good agreement is observed between the predicted (by DFT calculation) and
15 experimental (using the liquid phase IR-ATR study) vibrational frequencies of the pyridine
16 adsorption over silanol groups and Brønsted acid sites. In the high wavenumber zone (1650 –
17 1400 cm⁻¹), as expected, the bands observed at 1544 and 1490 cm⁻¹ were assigned to protonated
18 pyridine molecules over the Brønsted sites of the zeolites. Most notably, in the low frequency
19 zone (850 – 600 cm⁻¹) the experiments and DFT calculations allows establishing that the bands
20 observed at 750 and 703 cm⁻¹ correspond to H-bonded pyridine species whereas the bands at
21 727 and 686 cm⁻¹ can be assigned to pyridinium ions formed over the Brønsted acid sites of the
22 zeolites.

23 In the next section, the study of the adsorption and protonation of indole will be investigated
24 over the previously studied adsorbents. To go further, DFT calculations were performed in order
25 to predict expected frequencies according to the mode of interaction of indole with the surface.

26 **3.3 Indole Adsorption**

27 **3.3.1 IR-ATR Study of Liquid phase Indole Adsorption over the Solids**

1 Spectra corresponding to dissolved indole and indole adsorbed over HY2.5, USY33, and MCM-
2 41 in the high and low-wavenumber zones are presented in Figure 7. The IR-ATR spectrum of
3 liquid indole (dotted line) shows bands at 1455, 1414 cm^{-1} and a shoulder at 1468 cm^{-1} in the
4 high wavenumber zone as well as bands at 768, 763, 738 and 716 cm^{-1} in the low wavenumber
5 zone. The solution flowed over the ATR crystal contained indole diluted into hexane (0.5
6 wt.%). To obtain the indole spectrum, the bands of hexane must be eliminated by subtracting
7 the spectra of pure n-hexane. Since n-hexane presents intense bands at 1468 and 728 cm^{-1} , the
8 shoulders observed in the indole spectrum at these wavenumbers should correspond to partially
9 eliminated n-hexane bands after the subtraction. Thus, these two bands will not be considered in
10 the assignment of the indole bands.

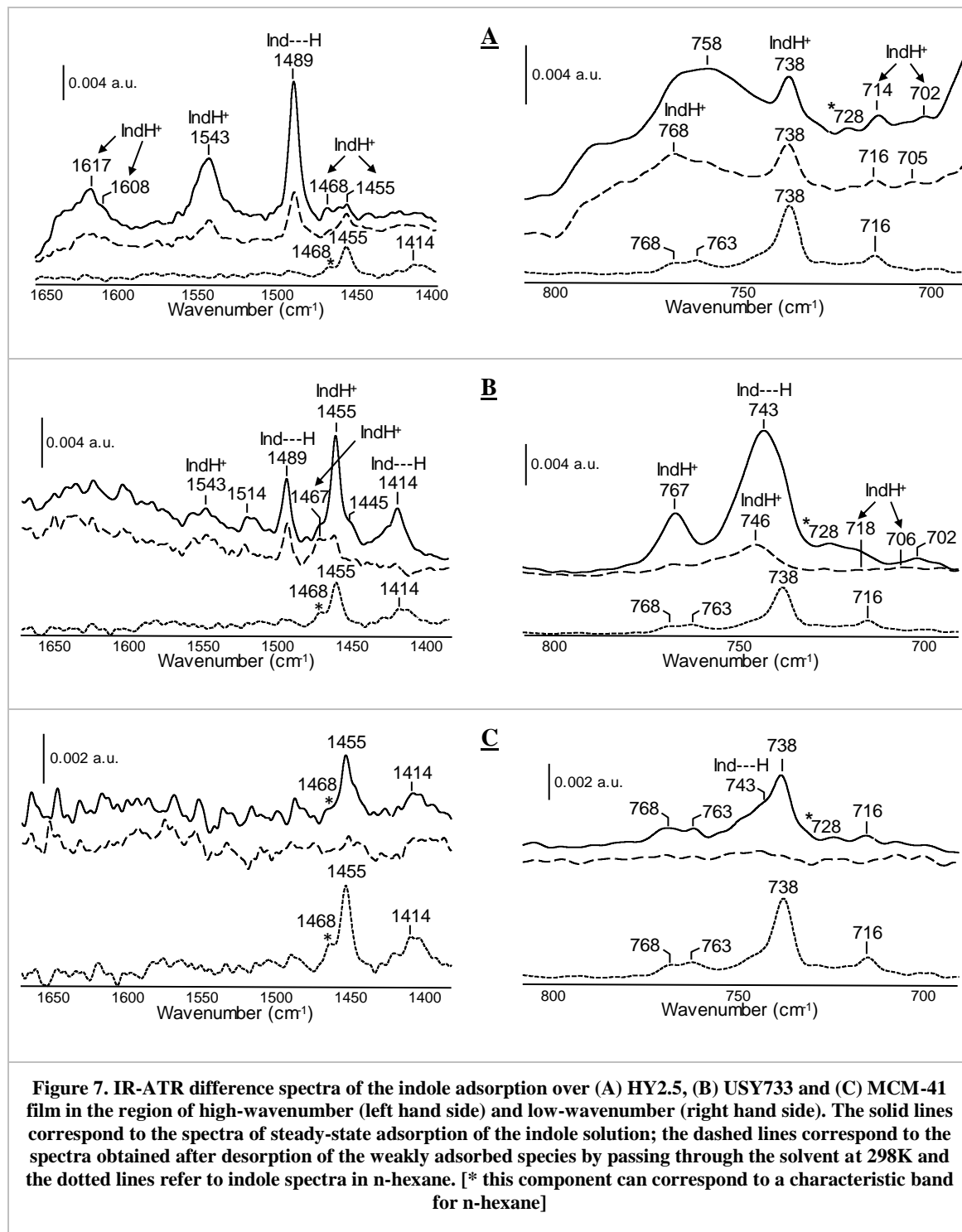
11 After indole adsorption over the HY2.5 zeolite film (Figure 7A), bands appear at 1617, 1608,
12 1543, 1489, and 1455 cm^{-1} , in the high-wavenumber zone. In the low-wavenumber zone, bands
13 are detected at \sim 758, 738, 716 and 702 cm^{-1} . However, a broad massif also appears at 787-750
14 cm^{-1} . As previously noticed for pyridine adsorption on HY2.5 (Figure 4), this massif was
15 attributed to the change in the frequency of the vibrations of the T-O-T bridges during the
16 indole adsorption. During desorption under n-hexane flow, most of these bands resist flushing
17 and remain present with lower intensities (dashed line).

18 The indole adsorption over the USY33 zeolite film (Figure 7B) shows new bands at 1543, 1514,
19 1489, 1455, and 1414 cm^{-1} in the high-wavenumber zone and 767, 743, 718, and 702 cm^{-1} in the
20 low-wavenumber zone. Most of these bands were observed on HY2.5 spectra even if with
21 different intensities. As previously shown over HY2.5, during the desorption most of these
22 bands lose intensity but withstand rinsing under the solvent flow. Only the band at 1414 cm^{-1}
23 disappears totally which allows to attribute it to weakly-adsorbed indole species (Figure 7B and
24 Figure 8). The zoom presented Figure 8 makes clearly visible that the bands at 728, 718 and 706
25 cm^{-1} resist to the n-hexane flush.

26 Over the MCM-41 film (Figure 7-C), bands at 1455, 1414 as well as 768, 763, 745, 738, and
27 716 cm^{-1} are observed. These bands are very close to those of liquid indole. Moreover, they

1 completely disappear after flowing hexane, which confirms that indole species are not strongly
 2 adsorbed over MCM-41.

3



4

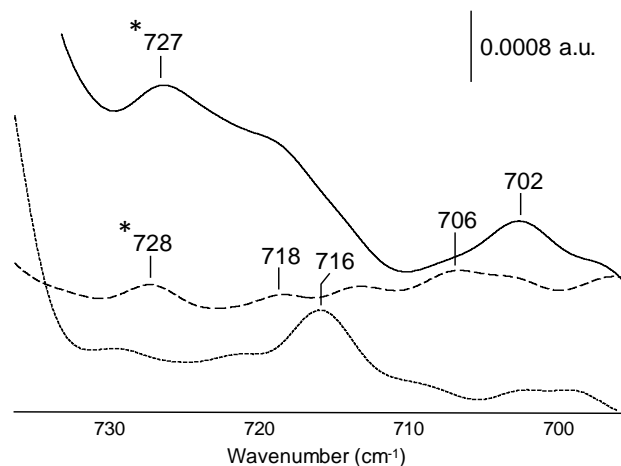
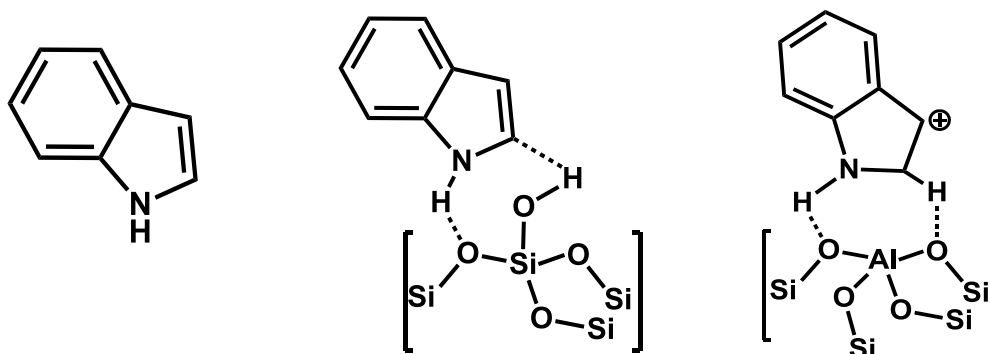


Figure 8. IR-ATR spectra of the indole adsorption over USY33 zeolite and of pure indole (Zoom of the Figure 7B - right). The solid line corresponds to the spectrum of the steady-state adsorption of the indole solution; the dashed line corresponds to the spectrum obtained after desorption of the weakly adsorbed species by passing through the solvent at 298K and the dotted line refers to indole spectrum in n-hexane. [* this component can correspond to a characteristic band for n-hexane]

1 3.3.2 Theoretical Assessment of the Adsorption of Indole

2 To assign the bands recorded on the IR-ATR spectra, DFT calculations of the vibrational
 3 frequencies of indole either in the gas phase or adsorbed on silanol or Brønsted acid sites were
 4 performed in the high and low-wavenumber zones. Indole can interact with the silanol group
 5 and with the zeolitic OH groups as depicted in Figure 9. The H-bonded interaction involves an
 6 interaction between the NH group of the indole molecule and the oxygen atom from the zeolite
 7 framework, as well as an interaction between the SiOH group and α -carbon of the C5 cycle. In
 8 such a configuration, the distance between the H of the SiOH group and the α -carbon is about
 9 1.95 Å. The most stable configuration of protonated indole was obtained over the carbon in
 10 position 3 (C3 site). A similar configuration was obtained by Somers *et al.*^[62]



Gas phase

Terminal silanol group

Brønsted acid site

Figure 9. The three evaluated configurations for the calculation of the vibrational frequencies for indole adsorption.

1 The predicted vibrational frequencies for indole in the gas phase, interacting with the silanol
2 group or with a protonated OH group of the zeolite were calculated and are reported in Table 4.

3 **Table 4. Comparison between the predicted vibrational frequencies and the experimental values obtained in**
4 **IR-ATR of the indole adsorption over a silanol group and a Brønsted acid site.**

Vibrational modes	Indole frequencies (cm ⁻¹)						
	Gas phase		Liquid phase	Silanol group		Brønsted acid site ^b	
	[Ref] ^a	This work (Calc.)	This work (IR-ATR)	This work (Calc.)	This work (IR-ATR)	This work (Calc.)	This work (IR-ATR)
In-Plane Quadrant and Semicircular Stretching of the rings	1614	1613	-	1615	1617	1623,1600	1617,1608
	1576	1575	-	1573	-	-	-
	-	-	-	-	-	1554	1543
	1505	1505	-	1496	1489	-	-
	1486	1485	-	1482	1489	1468	1468
	1456	1444	1455	1442	1445	1450	1455
	1415	1416	1415	1411	1414	-	-
Out-of-plane vibrations of the rings and H atoms	765	757	768	774	767	768	768
	747	755	763	758	-	740	738/746
	731	731	738	745	743	717	716
	719	709	716	737	-	-	-
	-	-	-	-	-	700	705

5 ^a OMNIC database, Aldrich Catalog No: I-340-8

6 ^b C3 protonated indole

7 For indole in the gas phase, the calculations predicted several bands in the region of high
8 frequencies; namely, 1613, 1575, 1505, 1485, 1444, and 1416 cm⁻¹. These bands are attributed
9 to in-plane vibrational modes of the 6 and 5-membered rings (Figure 10). In the region from 800
10 to 650 cm⁻¹, calculated vibrational modes corresponding to out-of-plane motions are predicted at
11 757, 755, 731, and 709 cm⁻¹.

12

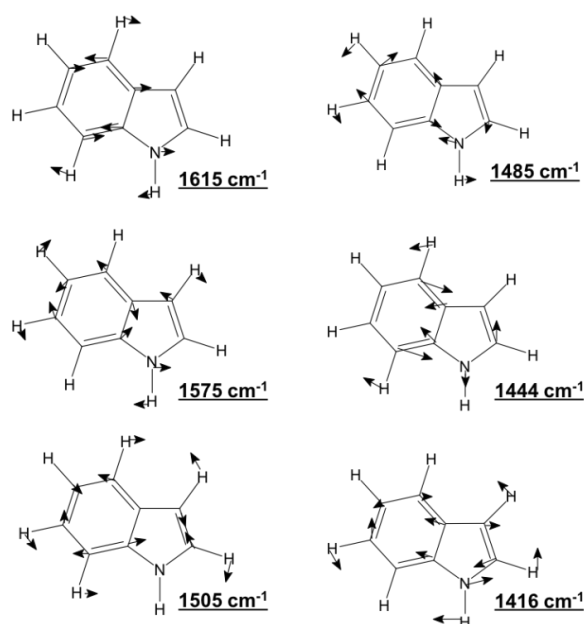


Figure 10. Atomic displacements for in-plane vibrational modes of indole in the gas phase in the region of 1400 to 1600 cm^{-1} .

1 Indole keeps the same atomic motions as in the gas phase and small shifts are predicted
 2 compared to gas-phase frequencies when the molecule is H-bonded to silanol groups. Table 4
 3 shows that H-bonded indole should give rise to bands at 1615, 1573, 1496, 1482, 1442, and
 4 1411 cm^{-1} in the high-wavenumber zone. Concerning the low-wavenumber zone, bands at 774,
 5 758, 745, and 737 cm^{-1} should be observed. On the contrary, for indole interacting with a
 6 Brønsted acid site, the calculations predicted shifts in the C-C stretching modes of the C5 and
 7 C6 cycles. This could be attributed to the change in the vibrational modes of the adsorbed
 8 molecule, even some additional modes can be predicted over the protonated atom (C3). Hence,
 9 the supplementary band at 1554 cm^{-1} corresponds to a C-C stretching vibration of the protonated
 10 carbon (sp^3) of the indole rings (Table 4). In the region of low-frequency, the theoretical
 11 calculation of indole on a Brønsted acid site has shown a new band at 700 cm^{-1} attributed to out-
 12 of-plane motions of the hydrogen atoms of the C5 cycle.

13 The vibrational frequencies predicted for gas-phase indole adsorbed on a silanol terminal group
 14 and a Brønsted site of a mordenite can be summarized as follows: (i) for the interactions of
 15 indole with silanol groups small shifts were obtained; (ii) for protonation of indole more
 16 important shifts are expected and new bands should appear. Next, the calculated vibration

1 frequencies were compared to the experimental spectra in order to assign the observed bands
2 and identify the indole adsorption modes on the different solids.

3 *Comparison between calculated and observed vibrational frequencies of indole*

4 The reference gas phase spectrum of indole (Figure SI-5, spectra from the Omnic database and
5 Table 4) presents bands at very similar wavenumbers to the computed ones. On the
6 experimentally IR-ATR spectrum of indole in the liquid phase (Figure 7), the most intense
7 bands are observed at 1455 cm^{-1} and 1414 cm^{-1} , while those at 1613 , 1575 , 1505 , and 1485 cm^{-1}
8 were not detected (Table 4). This is likely due to the low amount of indole in the n-hexane
9 mixture (0.5wt. %) and the low intensity of IR-ATR spectra.

10 A parallel between the computed vibrational frequencies (Table 4) and the recorded spectra of
11 indole on HY2.5 (Figure 7A) allows assigning the bands at 1617 , 1608 , and 1543 cm^{-1} to
12 protonated indole species. These protonated species were also detected on USY33 (Figure 7B),
13 however, the bands were less intense which agrees with the lower concentration of BAS over
14 the dealuminated USY zeolite (Table 2). The noisy spectra and the lower concentration of
15 protonated indole prevent the detection of the bands at 1617 and 1608 cm^{-1} on USY33. As
16 expected, the characteristic bands for protonated indole species were not detected on MCM-41.
17 The band at 1489 cm^{-1} detected on both HY2.5 and USY33 zeolites can be assigned
18 straightforwardly to H-bonded indole (Table 4), while the assignment of the bands at 1455 and
19 1468 cm^{-1} was not as obvious. Table 4 shows that the band at 1455 cm^{-1} can be characteristic for
20 both protonated indole and liquid phase indole, whereas the band at 1468 cm^{-1} can be assigned
21 to protonated indole or, alternatively, to the presence of residual n-hexane in the difference
22 spectrum, thus making difficult to assign these bands to a unique species.

23 In the low wavenumber zone, liquid indole presents four bands at 768 , 763 , 736 , 716 cm^{-1} ,
24 which matches satisfactorily with the calculated frequencies (Table 4). The main question to
25 answer when analyzing the low-wavenumber region is: does this spectral region confirm the
26 formation of protonated indole species on faujasites samples? Table 4 shows that a
27 characteristic band of protonated indole species should appear at about 700 cm^{-1} . First, it must

1 be underlined that the experimental spectrum of liquid indole or indole on MCM-41 does not
2 present any band at about 700 cm^{-1} (Figure 7C). On HY2.5, and similarly on USY33, Figure 7A
3 and Figure 7B (and more clearly the zoom presented in Figure 8) point out a weak band at 702
4 cm^{-1} which shifts to 705 cm^{-1} (706 cm^{-1} for USY33) after flowing with the solvent. Thus, both
5 high and low- wavenumber zones provide spectroscopic evidence for indole protonation
6 through the appearance of bands at 1543 cm^{-1} (as well as $1617, 1608\text{ cm}^{-1}$) and 705 cm^{-1} . The
7 other features detected at $767, 746\text{-}738,$ and 716 cm^{-1} both on HY2.5 and USY33 can support
8 indole protonation but can be also assigned to H-bonded indole.

9 Over the MCM-41 film (Figure 7-C), only the liquid indole bands were detected in the high
10 wavenumber zone. In the low-wavenumber zone, a small shoulder was observed at 745 cm^{-1}
11 attributed to weakly adsorbed indole molecules over a silanol group. All bands disappear after
12 flowing with n-hexane, which confirms the weak interaction of indole with the siliceous film.

13 Considering the collected evidence, this IR-ATR study reveals that indole, a weakly basic
14 compound, can be protonated on acidic Y zeolites as unambiguously evidenced by the
15 formation of the bands at $1617, 1608, 1543,$ and 705 cm^{-1} . In this way, Laredo *et al.* attempted
16 to separate basic from weakly basic nitrogenates in a heavy oil fraction by using solid acids.^[77]
17 The separation was not efficient, and this was ascribed to the strong adsorption of the weakly
18 basic compounds on the employed materials. Therefore, the interaction of indole with Brønsted
19 acid sites via the formation of an ion-pair complex is feasible, contrary to the suggested
20 mechanism of dissociative adsorption.^[78] Such interactions should also alter the surface
21 chemistry of these materials and thus block the Brønsted acid sites. These findings draw
22 attention to the possible role of weakly basic nitrogen compounds that can modify the catalytic
23 performance of zeolitic materials employed for hydrocracking units.^[4]

24 **4. CONCLUSIONS**

25 The interaction modes of liquid phase pyridine and indole over HY and USY zeolites and
26 MCM-41 solid films were successfully studied by using an *in situ* liquid-solid IR-ATR setup

1 and theoretical calculations. Using IR-ATR system offers two main advantages, it allows : (1)
2 the analysis of the low frequency region ($< 800 \text{ cm}^{-1}$) that presents characteristic vibrational
3 modes of adsorbed species, (2) studying the adsorption of low vapor pressure molecules (such
4 as indole) that presents an inherent difficulty to be operated in the gas phase IR cells.

5 A parallel between the vibrational frequencies predicted by DFT calculations, and the
6 experimental results obtained using the IR-ATR cell for studying of the solid films under
7 continuous liquid flow shows that:

8 - As for pyridine, the low wavenumber zone, a newly explored zone, can also account for its
9 adsorption modes. Indeed, the IR bands at 686 and 727 cm^{-1} characterize the pyridinium
10 species formed on zeolitic OH groups, while the signals at 703 and 750 cm^{-1} are associated
11 with pyridine in interaction with silanol groups.

12 - As for indole, the IR-ATR study points out the presence of new bands after its adsorption
13 over Y zeolites and MCM-41. Over the zeolites, the detection of bands at 1617 , 1608 , 1543
14 and 705 cm^{-1} provides evidence for the formation of protonated indole species over acidic
15 OH groups.

16 These findings support the fact that indole, a weakly basic nitrogenates, can be protonated over
17 the zeolitic acid sites and thus decreasing their activity during the hydrocracking process.

18 **ACKNOWLEDGMENTS**

19 The authors thank Yoann Levaque for helping in assembling the IR-ATR setup. Labex EMC3,
20 ANR and FEDER are also acknowledged for the PhD grant of IK and the financial support to
21 the BIOCAR project. Authors thank Ecopetrol S.A. for funding the present work through the
22 project AC2-5211770. The gentle collaboration of the SC3 work team from the GUANE
23 platform at UIS is acknowledged. VGBM thanks VIE-UIS and Colciencias are also thanks for
24 funding and for PhD grant of CMCC. The authors also thank Lille University Calculation center
25 (CRI) partially funded by FEDER for CPU allocation.

26

1 REFERENCES

- 2 [1] R. A. Santen, M. Neurock, *Wiley-VCH* **2006**, 474.
- 3 [2] G. H. C. Prado, Y. Rao, A. de Klerk, *Energy Fuels* **2017**, *31*, 14–36.
- 4 [3] M. Argyle, C. Bartholomew, *Catalysts* **2015**, *5*, 145–269.
- 5 [4] C. M. Celis-Cornejo, D. J. Pérez-Martínez, J. A. Orrego-Ruiz, V. G. Baldovino-
6 Medrano, *Energy Fuels* **2018**, *32*, 8715–8726.
- 7 [5] J. K. Minderhoud, J. A. R. van Veen, *Fuel Process. Technol.* **1993**, *35*, 87–110.
- 8 [6] C. M. Fu, A. M. Schaffer, *Ind. Eng. Chem. Prod. Res. Dev.* **1985**, *24*, 68–75.
- 9 [7] G. Adamski, K. Dyrek, A. Kotarba, Z. Sojka, C. Sayag, G. Djéga-Mariadassou,
10 *Catal. Today* **2004**, *90*, 115–119.
- 11 [8] P. Dufresne, A. Quesada, S. Mignard, *Elsevier* **1989**, 301–315.
- 12 [9] M. Kobayashi, S. Togawa, K. Ishida, *J. Jpn. Pet. Inst.* **2007**, *50*, 44–52.
- 13 [10] M. Sau, K. Basak, U. Manna, M. Santra, R. P. Verma, *Catal. Today* **2005**, *109*,
14 112–119.
- 15 [11] F. A. Barbosa, A. C. B. dos Santos, M. I. P. da Silva, A. M. Stumbo, *Catal. Today*
16 **2004**, *98*, 109–113.
- 17 [12] E. Furimsky, F. E. Massoth, *Catal. Today* **1999**, *52*, 381–495.
- 18 [13] W. R. Pitt, D. M. Parry, B. G. Perry, C. R. Groom, *J. Med. Chem.* **2009**, *52*, 2952–
19 2963.
- 20 [14] T. Nishida, H. Ida, Y. Kuninobu, M. Kanai, *Nat. Commun.* **2014**, *5*, 1–6.
- 21 [15] L. N. Obasi, U. S. Oruma, I. A. Al-Swaidan, P. Ramasami, C. J. Ezeorah, A. E.
22 Ochonogor, *Molecules* **2017**, *22*, 153–163.
- 23 [16] D. Hédou, J. Godeau, N. Loaëc, L. Meijer, C. Fruit, T. Besson, *Molecules* **2016**,
24 *21*, 578–596.
- 25 [17] M. D. Altintop, Ö. D. Can, Ü. D. Demir Özkay, Z. A. Kaplancikli, *Molecules*
26 **2016**, *21*, 1004–1013.
- 27 [18] S. Su, X. Zhou, G. Liao, P. Qi, L. Jin, *Molecules* **2017**, *22*, 64–80.
- 28 [19] D. V. Gopal, B. Srinivas, V. Durgakumari, M. Subrahmanyam, *Appl. Catal., A*
29 **2002**, *224*, 121–128.
- 30 [20] M. Karthik, A. Tripathi, N. Gupta, M. Palanichamy, V. Murugesan, *Catal.*
31 *Commun.* **2004**, *5*, 371–375.
- 32 [21] M. W. Roomi, S. F. MacDonald, *Can. J. Chem.* **1969**, *48*, 139–143.
- 33 [22] X. Zhao, Y. Jia, J. Li, R. Dong, J. Zhang, C. Ma, H. Wang, Y. Rui, X. Jiang, *ACS*
34 *Appl. Mater. Interfaces* **2018**, *10*, 29398–29406.
- 35 [23] F. Thibault-Starzyk, F. Maugé, *Wiley* **2012**, *Chapter 1*, 1–48.
- 36 [24] J. Ryczkowski, *Catal. Today* **2001**, *68*, 263–381.
- 37 [25] Pa. Meulen, R. F. Mann, *J. Am. Chem. Soc.* **1931**, *53*, 451–453.
- 38 [26] J.-M. Andanson, A. Baiker, *Chem. Soc. Rev.* **2010**, *39*, 4571–4584.

- 1 [27] D. Rivera, J. M. Harris, *Langmuir* **2001**, *17*, 5527–5536.
- 2 [28] A. Davantès, D. Costa, B. Sallman, S. Rakshit, G. Lefèvre, *J. Phys. Chem. C* **2017**,
3 *121*, 324–332.
- 4 [29] I. A. Mudunkotuwa, A. A. Minshid, V. H. Grassian, *Analyst* **2014**, *139*, 870–881.
- 5 [30] B. Panella, A. Vargas, D. Ferri, A. Baiker, *Chem. Mater.* **2009**, *21*, 4316–4322.
- 6 [31] K. Grabow, U. Bentrup, *ACS Catal.* **2014**, *4*, 2153–2164.
- 7 [32] M. Chen, N. Maeda, A. Baiker, J. Huang, *ACS Catal.* **2012**, *2*, 2007–2013.
- 8 [33] C. Keresszegi, D. Ferri, T. Mallat, A. Baiker, *J. Phys. Chem. B* **2005**, *109*, 958–
9 967.
- 10 [34] A. J. Wain, M. A. O’Connell, G. A. Attard, *ACS Catal.* **2018**, *8*, 3561–3570.
- 11 [35] D. Ferri, T. Bürgi, A. Baiker, *J. Phys. Chem. B* **2001**, *105*, 3187–3195.
- 12 [36] J. E. Pander, M. F. Baruch, A. B. Bocarsly, *ACS Catal.* **2016**, *6*, 7824–7833.
- 13 [37] M. F. Baruch, J. E. Pander, J. L. White, A. B. Bocarsly, *ACS Catal.* **2015**, *5*, 3148–
14 3156.
- 15 [38] N. S. Gould, B. Xu, *ACS Catal.* **2018**, *8*, 8699–8708.
- 16 [39] J. Lomratsiri, M. Probst, J. Limtrakul, *J. Mol. Graphics Modell.* **2006**, *25*, 219–
17 225.
- 18 [40] C. Liu, G. Li, E. J. M. Hensen, E. A. Pidko, *J. Catal.* **2016**, *344*, 570–577.
- 19 [41] J. Meeprasert, S. Jungstittiwong, S. Namuangruk, *Microporous Mesoporous*
20 *Mater.* **2013**, *175*, 99–106.
- 21 [42] M. Castella Ventura, E. Kassab, Y. Akacem, *J. Phys. Chem. C* **2008**, *112*, 19045–
22 19054.
- 23 [43] M. Grün, K. K. Unger, A. Matsumoto, K. Tsutsumi, *Microporous Mesoporous*
24 *Mater.* **1999**, *27*, 207–216.
- 25 [44] S. Brunauer, P. H. Emmett, E. Teller, *J. Am. Chem. Soc.* **1938**, *60*, 309–319.
- 26 [45] M. Kruk, M. Jaroniec, C. H. Ko, R. Ryoo, *Chem. Mater.* **2000**, *12*, 1961–1968.
- 27 [46] M. Maache, A. Janin, J. C. Lavalley, E. Benazzi, *Zeolites* **1995**, *15*, 507–516.
- 28 [47] S. Chibani, M. Chebbi, S. Lebègue, T. Bučko, M. Badawi, *J. Chem. Phys.* **2016**,
29 *144*, 244705–244714.
- 30 [48] J. Hafner, L. Benco, T. Bučko, *Top. Catal.* **2006**, *37*, 41–54.
- 31 [49] T. Barzetti, E. Selli, D. Moscotti, L. Forni, *J. Chem. Soc., Faraday Trans.* **1996**,
32 *92*, 1401.
- 33 [50] C. Liu, I. Tranca, R. A. van Santen, E. J. M. Hensen, E. A. Pidko, *J. Phys. Chem.*
34 *C* **2017**, *121*, 23520–23530.
- 35 [51] G. Kresse, J. Hafner, *Phys. Rev. B* **1993**, *48*, 13115–13118.
- 36 [52] G. Kresse, J. Hafner, *Phys. Rev. B* **1994**, *49*, 14251–14269.
- 37 [53] G. Kresse, J. Furthmüller, *Comput. Mater. Sci.* **1996**, *6*, 15–50.
- 38 [54] G. Kresse, D. Joubert, *Phys. Rev. B* **1999**, *59*, 1758–1775.

- 1 [55] E. P. Hessou, W. G. Kanhounon, D. Rocca, H. Monnier, C. Vallières, S.
2 Lebègue, M. Badawi, *Theor. Chem. Acc.* **2018**, *137*, 161–172.
- 3 [56] J. P. Perdew, K. Burke, M. Ernzerhof, *Phys. Rev. Lett.* **1996**, *77*, 3865–3868.
- 4 [57] S. Grimme, S. Ehrlich, L. Goerigk, *J. Comput. Chem.* **2011**, *32*, 1456–1465.
- 5 [58] X. Rozanska, R. A. van Santen, F. Hutschka, J. Hafner, *J. Am. Chem. Soc.* **2001**,
6 *123*, 7655–7667.
- 7 [59] C. M. Celis-Cornejo, M. M. Garnica Mantilla, V. G. Baldovino-Medrano, G. E.
8 Ramírez-Caballero, *J. Phys.: Conf. Ser.* **2016**, *743*, 12010–12016.
- 9 [60] T. Demuth, J. Hafner, L. Benco, H. Toulhoat, *J. Phys. Chem. B* **2000**, *104*, 4593–
10 4607.
- 11 [61] T. Bucko, L. Benco, Th. Demuth, J. Hafner, *J. Chem. Phys.* **2002**, *117*, 7295–
12 7305.
- 13 [62] K. R. F. Somers, E. S. Kryachko, A. Ceulemans, *Chem. Phys.* **2004**, *301*, 61–79.
- 14 [63] I. Khalil, H. Jabraoui, G. Maurin, S. Lebègue, M. Badawi, K. Thomas, F. Maugé,
15 *J. Phys. Chem. C* **2018**, *122*, 26419–26429.
- 16 [64] R. López-Fonseca, J. I. Gutiérrez-Ortiz, M. A. Gutiérrez-Ortiz, J. R. González-
17 Velasco, *J. Catal.* **2002**, *209*, 145–150.
- 18 [65] I. Fornefett, D. Rabet, C. Buttersack, K. Buchholz, *Green Chem.* **2016**, *18*, 3378–
19 3388.
- 20 [66] I. Khalil, K. Thomas, H. Jabraoui, P. Bazin, F. Maugé, *J. Hazard. Mater.* **2019**,
21 *Just accepted*.
- 22 [67] J. N. Kondo, R. Nishitani, E. Yoda, T. Yokoi, T. Tatsumi, K. Domen, *Phys. Chem.*
23 *Chem. Phys.* **2010**, *12*, 11576.
- 24 [68] G. Poncelet, *J. Catal.* **1978**, *52*, 321–331.
- 25 [69] T. K. Phung, M. M. Carnasciali, E. Finocchio, G. Busca, *Appl. Catal., A* **2014**,
26 *470*, 72–80.
- 27 [70] H. Jabraoui, I. Khalil, S. Lébegue, M. Badawi, *Mol. Syst. Des. Eng.* **2019**, *4*, 882–
28 892.
- 29 [71] S. Khabtou, T. Chevreau, J. C. Lavalley, *Microporous Mater.* **1994**, *3*, 133–148.
- 30 [72] L. M. Parker, D. M. Bibby, G. R. Burnst, *J. Chem. Soc., Faraday Trans.* **1991**, *87*,
31 3319–3323.
- 32 [73] E. Spinner, *J. Chem. Soc.* **1963**, 3870–3873.
- 33 [74] E. B. Wilson, *Phys. Rev.* **1934**, *45*, 706–714.
- 34 [75] R. Ferwerda, J. H. van der Maas, F. B. van Duijneveldt, *J. Mol. Catal. A: Chem.*
35 **1996**, *104*, 319–328.
- 36 [76] L. Kubelkova, J. Kotrla, J. Florian, *J. Phys. Chem.* **1995**, *99*, 10285–10293.
- 37 [77] G. C. Laredo, S. Leyva, R. Alvarez, M. T. Mares, J. Castillo, J. L. Cano, *Fuel*
38 **2002**, *81*, 1341–1350.
- 39 [78] M. A. Larrubia, A. Gutiérrez-Alejandre, J. Ramirez, G. Busca, *Appl. Catal., A*
40 **2002**, *224*, 167–178.
- 41

